A COMPARISON OF INFRARED, RADAR, AND GEOLOGIC MAPPING OF LUNAR CRATERS*

T. W. THOMPSON
Jet Propulsion Laboratory, Pasadena, Calif., U.S.A.
H. MASURSKY
United States Geological Survey, Flagstaff, Ariz., U.S.A.
R. W. SHORTHILL**
Boeing Aerospace Company, Seattle, Wash., U.S.A.
G. L. TYLER
Stanford University, Palo Alto, Calif, U.S.A.
and
S. H. ZISK
MIT Haystack Observatory, Westford, Mass., U.S.A.

(Received 30 June, 1973)

Abstract. Between 1000 and 2000 infrared (eclipse) and radar anomalies have been mapped on the nearside hemisphere of the Moon. A study of 52 of these anomalies indicates that most are related to impact craters and that the nature of the infrared and radar responses is compatible with a previously developed geologic model of crater aging processes. The youngest craters are pronounced thermal and radar anomalies; that is, they have enhanced eclipse temperatures and are strong radar scatterers. With increasing crater age, the associated thermal and radar responses become progressively less noticeable until they assume values for the average lunar surface. The last type of anomaly to disappear is radar enhancement at longer wavelengths. A few craters, however, have infrared and radar behaviors not predicted by the aging model. One previously unknown feature – a field strewn with centimeter-sized rock fragments – has been identified by this technique of comparing maps at the infrared, radar, and visual wavelengths.

1. Introduction

The previous articles in this series emphasized the measurement of lunar scattering, the techniques of measurements, and the results at wavelengths of 70 and 3.8 cm. This article will emphasize the correlation of the radar mappings with other data sets, particularly the infrared and geologic mapping of the Moon.

Remotte sensing of the Moon at infrared and radar wavelengths has resulted in maps with resolutions (1–15 km) comparable to those of topographic and geologic maps produced from visual observations. However, there has been little previous

* A major portion of this paper was written during June 1970 at the working symposium on the geophysical interpretation of the Moon, Lunar Science Institute, Houston, Texas, chaired by Eugene Simmons of the Massachusetts Institute of Technology. The paper is Contribution No. 16 of The Lunar Science Institute, which is supported under Universities Space Research Association, Charlottesville, Virginia, and the National Aeronautics and Space Administration Manned Spacecraft Center, Contact No NSR 09-051-001.
** Now at University of Utah Research Institute, Salt Lake City, Utah 84112.

The Moon **10** (1974) 87–117.

comparison between the behavior of lunar features observed at these different wavelengths (Hafors, 1970). We have attempted to do this by considering the possible lunar surface conditions implied by the infrared and radar observations. Only a few of these conditions could have remained on a lunar surface composed of fragmental debris acted upon by meteoritic bombardment. The rate of occurrence of various combinations of infrared and radar behavior and the detailed behavior of particular craters types may be predicted. These predictions were tested with 52 lunar craters, which were chosen from the radar and infrared maps by various criteria described below. There are 1000 to 2000 infrared and radar anomalies; however, we feel that the craters selected for study are representative.

The observables, the eclipse thermal emissions and radar backscatter, are controlled in large part by the abundance and size of discrete rock fragments occurring on the surface or buried at slight depth. (For reasons of convenience, discrete fragments of cohesive material will be referred to as 'rocks'. The term will be applied to all fragments 1 cm or larger in size, regardless of their shape or composition.) An infrared anomaly, an area which maintains an elevated temperature during the umbral phase of an eclipse, requires an excess of exposed rocks more than 10 cm in diam (Winter, 1970). A radar anomaly, an area of enhanced radar backscatter, requires an excess of wavelength-sized rocks exposed on the surface or buried no deeper than 5 wavelengths. (This problem has been considered by a number of authors. See, for example, Burns, 1969; Campbell and Ulbricht, 1969; Hagfors, 1967; Thompson *et al.*, 1970; Tyler, 1968.) At the resulution employed, these areas of excess rocks must be at least 1 to 10 km in diam to be observed.

Most of the lunar surface is a thin layer of poorly sorted unconsolidated rock debris – the regolith – which overlies consolidated bedrock. The origin and modification of the regolith by meteoritic bombardment have been discussed in detail by several authors (for example, Oberbeck and Quaide, 1968; Quaide and Oberbeck, 1968; Shoemaker and Morris, 1970; Shoemaker, *et al.*, 1970a, b; and Gault, 1970).

Most of the localized infrared and radar anomalies are associated with young impact craters. Photogeologic interpretation of visual images has demonstrated that young impact craters contain abundant blocks of ejected bedrock on their floors, walls, and rims. Further, rock fragments decrease in size and frequency of occurrence with increasing age of the parent crater. This relationship is attributed to lunar aging processes, due largely to continuing bombardment.

Our purpose in this paper is to determine if the variation in the radar and infrared response of different craters is consistent with the gelogic interpretation of crater age. The basic infrared, radar, and geologic mapping data are reviewed in Section 2; in Section 3, a truth table for the interpretation of infrared and radar anomalies is presented, and in Section 4, the infrared, radar, and geologic characteristics of 52 craters are compared.

2. Infrared, Radar, and Geologic Mapping

We will compare three data sets – eclipse temperatures at a wavelength of 11 μ and

radar backscatter at 3.8- and 70-cm wavelengths – with the relative crater ages deduced from regional and detailed geologic mapping studies.

A. INFRARED MAPPING: A BRIEF REVIEW

The thermophysical properties of the lunar surface are studied by measuring the thermal emission from the Moon at infrared wavelengths. Groundbased measurements are limited mainly to wavelengths of 8 to 14 μ and 17 to 24 μ because of atmospheric absorption. Most measurements have been made in the 8–14 μ window and in particularly narrow bands of this window.

The brightness temperature of the sunlit lunar surface is controlled by insolation, surface roughness, and albedo. The latter two properties are noticeably affected by surface rock populations. The thermal response of the lunar nighttime surface is difficult to measure from the Earth because of the low brightness temperatures (about 100 K) of the Moon. At present, Earth-based observation times of hours are required to scan an appreciable portion of the surface. The recent Apollo 17 has very successfully measured the thermal response of the nighttime surface, showing thermal structure that correlates in some cases with the eclipse results. The higher resolution, however, results in much fine detail (Low and Mendell, 1973) which is not resolved in the Earth-based measurements.

The thermal response of the lunar surface can be measured easily from the Earth during an eclipse when the average surface cools from the full Moon temperature of about 400 K to about 150 K. With this higher background temperature, the entire disk can be scanned quickly at high resolution. The eclipse measurements of Shorthill and Saari, which are used here, have been reviewed by Shorthill (1970). The Moon was scanned four times during the penumbral phase of the lunar eclipse of December 19, 1964, by a mercury-doped germanium photodetector cooled with liquid neon. Each scan took 17 min, and a resolution of 10″ was achieved. A wavelength of 11 μ minimized the effects of the atmospheric water vapor bands. The necessary equipment was mounted at the Newtonian focus of a large-aperture telescope, and the detector was moved across the focal plane in a rectangular raster. In the subsequent data reduction, selenographic positions of the scans were determined by associated small lunar features with observed anomalies.

In order to compare different areas of the Moon on an equal basis, these data were normalized to the average behavior of the terrae (Shorthill *et al.*, 1970; Shorthill, 1973). This procedure removed the decrease in the temperature toward the limbs casued by the initial full-Moon temperature distribution and the asymmetry in the cooling time caused by the passage of the Earth's shadow across the disk. This normalization produced a 'flattened Moon' quantity ΔFM, given by

$$\Delta FM = \frac{(T_{\text{observed}} - T_{\text{base}})}{T_{\text{full Moon}}} \tag{1}$$

where T_{observed} is the observed temperature, T_{base} is the expected localised background temperature, and $T_{\text{full Moon}}$ is the localized full Moon temperature.

More than 1000 localized anomalies (hot spots) were observed (Shorthill and Saari, 1965). Entire maria and portions of maria also showed anomalous thermal behavior. However, a study has revealed that most hot spots are associated with craters or regions of high albedo and a few with areas of small clustered craters. The hot spots are not uniformly distributed over the lunar disk. A study of 300 hot spots indicated that two-thirds occur in the lunar maria and one-third in the uplands (Shorthill, 1970); the largest concentrations are found in Mare Tranquillitatis and in a region of Oceanus Procellarum between Kepler and Artistarchus.

An excess population of bare surface rocks has been suggested as the cause of these anomalies. Roelof (1968), Winter (1970) and Allen (1971) have shown that the increased temperatures of the hot spots can be explained by the thermal behavior of surface rocks. These studies show that surface rocks must be 10 cm or larger, and the number of surface rocks per unit area must be greater than that observed at the Surveyor 1 and 3 landing sites.

B. RADAR MAPPING: A BRIEF REVIEW

In contrast to infrared mapping, which measures natural thermal emissions from the lunar surface, radar mapping measures the response of the lunar surface to the man-made emissions of electromagnetic energy at radio wavelengths.

The radar scattering behavior of the Moon is examined by illuminating the Moon with electromagnetic energy and observing the scattered power in various directions. The polarization of the transmitted wave is carefully controlled, and usually two orthogonal polarizations are recorded. If the transmitter and receiver are at the same location, then the radar method is termed monostatic and only backscattered power is measured. Rather complete experiments of this type have been carried out at several wavelengths in the centimeter to meter range (Hagfors, 1970). With the advent of spacecraft, however, the transmitter and receiver can be widely separated. This method, termed bistatic, can be used to measure the forward scattering characteristics of the surface. These bistatic measurements are reviewed elsewhere (Tyler, 1968; Tyler and Simpson, 1970; Tyler and Howard, 1973).

Only mappings of backscatter by monostatic radars (described in the previous articles) will be considered here. These measurements use the delay-Doppler technique, which is described in the first article of this series. To reveal subtle differences in the scattering properties of different areas, the observed echoes are normalized to remove expected large-scale variations. Variations from both antenna gain and resolution area (which both vary with delay and frequency) are removed. Further normalization removes the mean scattering behavior, which is strongly dependent on the angle of incidence (the angle between the surface normal and the radar line of sight). Typically, variations of one order of magnitude result from the antenna and area effects, while variations of three to four orders of magnitude result from mean scattering behavior.

After normalization, the radar echoes are still nonuniform for several important physical reasons. Since lunar backscatter always decreases with increasing angle of incidence, areas tilted toward the radar exhibit enhancements. Such enhancements are

often observed at the rims of craters and on mountain sides and give a vivid illusion of highlights and shadows in the radar maps. Besides this tilt effect, radar scattering differences are also associated with important physical characteristics such as dielectric constant and surface roughness. While the radar signatures for these properties are subject to debate, we attribute an increase to radar backscatter to an increase in the number of dielectric discontinuities which have sizes on the order of the radar wavelength. Rock fragments are an excellent source of such discontinuities. Surface rocks will produce stronger enhancements than buried rocks. Rocks in the regolith cause enhancements if they are buried no deeper than 10 to 30 wavelengths (Campbell and Ulrichs, 1969). Thus if tilt can be eliminated as a source of scattering difference, then the enhancement of radar echoes is a measure of the population of wavelength-sized fragments lying on the surface or buried no deeper than 10 to 30 wavelengths.

Differentiation between the effects of tilt and roughness is facilitated by observations in different polarizations. The radar maps of this study were made by transmitting circularly polarized radiation of one sense and observing echoes in both left- and right-hand circular polarizations. We will follow the usual notation (Hagfors, 1967) and call these the polarized and depolarized echoes. (In many radar reports, the term 'expected' is used instead of the term 'polarized', which we use here.) Polarized echoes are in the polarization expected from a plane conducting target. They are strong near the subradar point and decrease sharply in strength with an increase in the angle of incidence, somewhat analogously to the optical glint of a shiny sphere. Depolarized echoes are in the polarization orthogonal to the polarized echoes. The average depolarized echo power per unit surface area varies as the cosine of the angle of incidence. Dpolarized backscattering is thought to be due to sharp-featured roughness on the scale of the radar wavelength such as the wavelength-sized rocks mentioned above (Hagfors, 1967). Only enhancements of depolarized echoes are considered here.

Rock size is important. Rocks smaller than one-quarter wavelength will be in the Rayleigh regime, where backscatter power decreases as the inverse fourth power of rock size. Larger rocks will tend to be smooth on the scale of a wavelength and will not contribute to depolarized echoes. Although it is difficult to establish a well-defined upper limit for rock size, we believe that rocks detected by radar will span the range from about one-quarter wavelength to about 10 wavelengths. Only the radar maps given in the previous articles, the 3.8 and 70 cm data, will be considered here. Thus, our criterion for the detection of rock populations implies that the 3.8-cm radar detects rocks which range in size from 1 to 40 cm and are on the surface or buried no deeper than about 1 meter. Similarly, the 70-cm radar detects those rocks which range in size from 20 cm to 7 m and are on the surface or buried no deeper than about 20 meters.

C. GEOLOGIC MAPPING: A BRIEF REVIEW

Whereas infrared and radar maps portray physical properties of lunar surface materials at nonvisual wavelengths, geologic maps portray a wide variety of features and properties observed in the visible part of the spectrum. In further contrast, geologic mapping places less emphasis on the direct measurement of physical prop-

erties and more emphasis on genetic and historical interpretation. The origin and relative age of lunar features and the evolutionary history of the lunar crust are deduced – largely by analogy with geologic conditions on Earth and by application of superposition and intersection.

These principles were first applied to the Moon in the southern part of the Mare Imbrium basin. By means of telescopic observation, a stratigraphic sequence was deduced by Shoemaker (1961, 1962) and Shoemaker and Hackman (1962) in the Copernicus-Eratosthenes area. Later workers, Carr (1964), Hackman, (1966), McCauley (1967), Schmitt *et al.*, (1967 and Wilhelms (1970), have amplified the stratigraphic relationships originally proposed. Based largely on considerations of superposition, the succession of major events which occurred in or near the southern part of the Imbrium basin are listed in Table I. Following stratigraphic convention, these events are listed from youngest (at the top) to oldest (at the bottom).

Systematic geologic mapping of most of the lunar nearside has since proven the validity of the original approach and the widespread applicability of the time-stratigraphic column originally proposed. The successful extension of the mapping effort across most of the lunar nearside and subsequent refinements in mapping techniques were in large part due to an increased understanding of the morphologic evolution of craters under the influence of lunar erosional and aging processes.

Detailed knowledge of crater form became possible only with the progressively improved resolution of the imaginary provided by the successive lunar exploration programs. Resolution of the best-Earth-based telescopic photographs ranged from 1

TABLE I

Stratigraphic relationship of major lunar events

Event	Stratigraphic relationships	Geologic period
Copernicus impact	Formation of ejecta deposits which overlie all older units, including those of crater Eratosthenes	Copernican
Eratosthenes impact	Formation of ejecta deposits which overlie all older units, including mare materials	Eratosthenian
Flooding of Imbrium basin and vicinity by mare materials	Mare material inundated a large part of lunar surface, embayed (overlap) rim of Imbrium basin, and covered most of the rim deposits of crater Archimedes	Imbrian
Archimedes impact	Formation of ejecta deposits which overlie all older units, including Apennine Bench Formation	
Deposition of Apennine Bench Formation – a light plains-forming unit unit probably composed of pyroclastic debris	Blankets part of the rim structure of the Imbrium basin; locally overlies the Fra Mauro Formation	Pre-Imbrian
Imbrium basic impact	Formation of huge blanket of ejecta (Fra Mauro Formation) which overlies pre-Imbrian terrain; uplifted rim forms Apennine Mountains; radial structures intersect pre-existing structures	

to 0.25 km. Some Lunar Orbiter photographs are resolvable to 1 m; Ranger pictures are resolvable to less than 1 m in very small areas; and Surveyor pictures range down to 1 mm in resolution in the immediate vicinity of the camera. The relationships between image resolution, limit of detectability, and crater size have been discussed by Keene (1965) and Masursky *et al.* (1970).

Many workers have contributed significantly to our concepts of the occurrence, origin, and evolution of lunar craters. Among the more significant contributors are the following: Gilbert (1893) attributed all craters – including the Imbrium basin – to the impact of meteorites, asteroids, and comets. Spurr (1948), on the other hand, proposed that all craters were formed by volcanic activity. Most recent students accept both types of origin but agree that the impact craters preponderate. For example, Masursky (1968) and Kosofsky and El-Baz (1970) have demonstrated that both are present. In addition, a third type of crater is now recognized (Kuiper, 1965). Called dimple craters, they are small in size and commonly thought to form by drainage or collapse of surface material into the substrate. Oberbeck, (1970) has recently proposed another origin for these dimple craters. Discussions related to the change in crater form with age – a process known as 'aging', 'degradation', or 'subdual' – have been presented by Dietz (1946), Baldwin (1949, 1963), Khabakov (1949), Hartmann and Kuiper (1962), Dodd *et al.* (1963), Kuiper *et al.* (1966), Quaide and Oberbeck (1967, 1969), Sukhanov *et al.* (1967), Trask (1967), Guest and Murray (1969), Gault (1970). In a definitive treatment by Pohn and Offield (1970), crater age and morphology are related within specific crater size intervals. These authors demonstrate that continuums of form exist from the youngest to the oldest craters before complete degradation.

The following geologic criteria are most commonly used to identify young impact craters, although they are not equally applicable to craters of all sizes. Perhaps most obvious is the 'fresh', bright (high albedo) appearance of young craters. Young craters are further characterized by sharp, irregular, almost jagged raised rim crests, steep interior walls, and a prominent central peak in moderate-sized (25–45 km) and large craters (>45 km). A prominently patterned, hummocky raised rim composed of ejected material is also characteristic. The rim deposits typically extend outward 1 to 2 crater diameters from the rim crest. Large angular rock fragments (blocks) are abundant in the ejecta; they are largest and most numerous near the rim crest but are also present on the walls and the floor. The ejecta blanket forming the rim thins outward and grades imperceptibly into a broad annular belt composed or bright rays and numerous loops and lines of secondary craters formed by the impact of large clots of ejected material. The rays may extend 30–35 diameters outward from the rim crest.

Immediately after an impact event, lunar erosional processes – largely in response to the continued bombardment of projectiles (meteorites and micrometeorites) – begin to operate. Given sufficient time, the crater features described above are destroyed or buried in approximately the following order. First to disappear are the bright rays, which assume the albedo of the underlying strata. Next are the clusters of secondary craters, which are leveled by subdual of their rims and filling of their interiors. Continued meteorite and micrometeorite bombardment and mass wasting triggered

by seismic shaking subdue the rim deposits. The characteristic hummocky texture disappears and the rim becomes progressively more subdued and the rim crest more rounded as the crater is gradually filled by material slumping off the rim and by ballistically transported ejecta from subsequent impact craters. Blanketing by volcanic debris is another process that tends to degrade craters.

Pertinent to this discussion is the aging history of the blocks of cohesive rock that constitute much of the ejecta of young impact craters. Study of Lunar Orbiter, Ranger, and Surveyor photographs has shown that rocks are normally inconspicuous around old craters. Where angular rock fragments are abundant around old craters, it can be shown that they are ballistically transported debris from younger craters or that they are previously buried fragments that have been exhumed by local winnowing processes. Morris *et al.* (1968) and Shoemaker and Morris (1970) analyzed in detail the shapes and sizes of rocks at several Surveyor sites. They concluded that erosional processes – largely the continued bombardment by meteorite and lunar debris – caused rounding of originally angular fragments, reduced them to size, and buried them to varying depths.

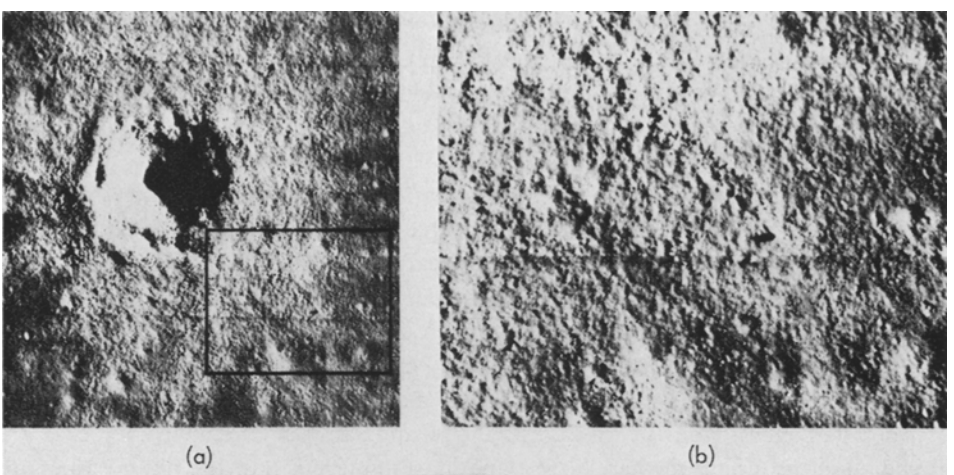

Fig. 1. (a) A small (500-m-diam), young, impact crater surrounded by blocky ejecta (43.9°W, 2.5°S; Lunar Orbiter III photograph H-189). (b) Enlargement of Figure 1a showing some of the ejecta southwest of the crater.

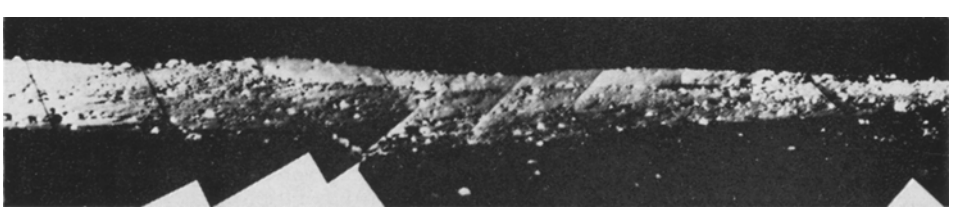

Fig. 2. Blocky ejecta on and near the rim of a crater near Surveyor 1 landing site.

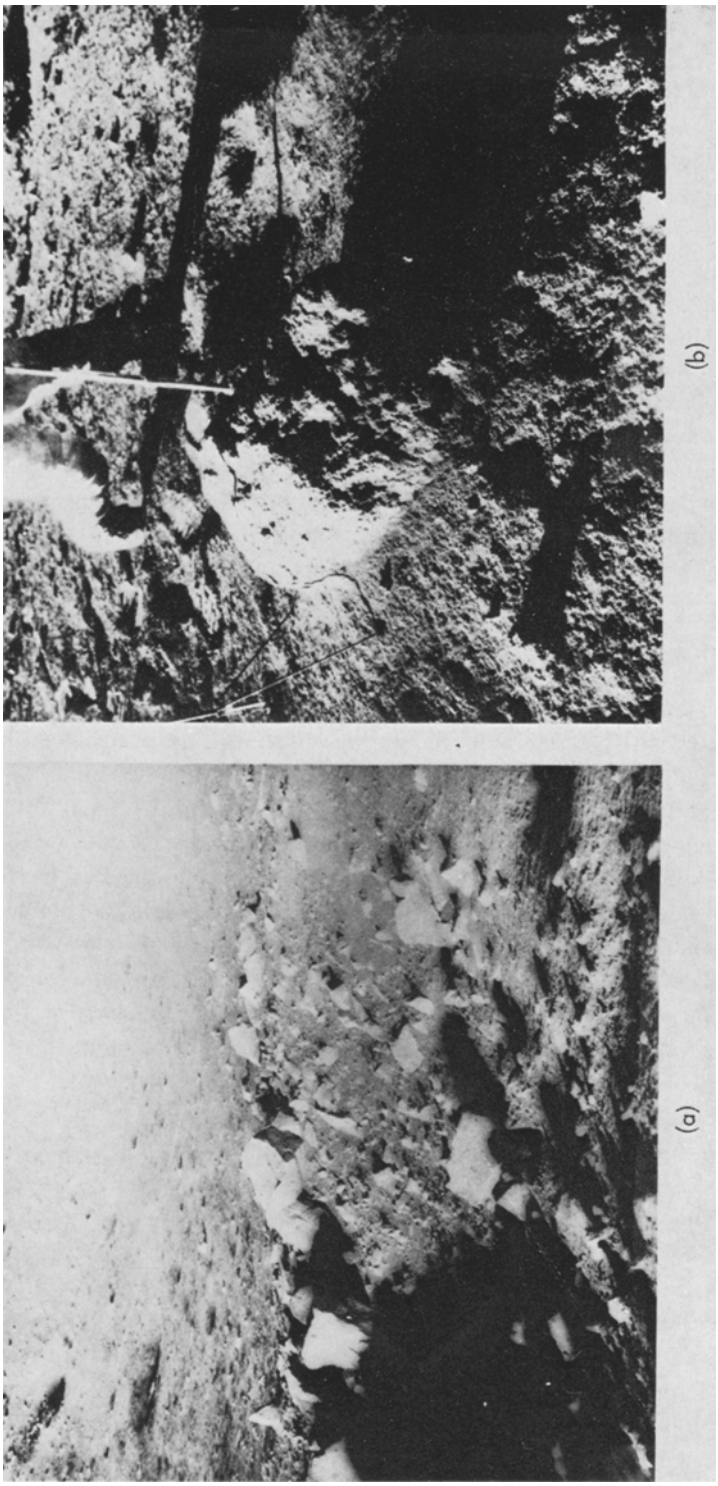

Fig. 3. (a) Young, angular, meter-sized block observed by Apollo 12 astronauts at Bench Crater (NASA photograph AS12-48-7146). (b) Older, subangular, meter-sized block observed by Apollo 12 astronauts (NASA photograph AS12-48-7062).

Rocks have been observed in many Orbiter, Surveyor, and Apollo photographs. For example, a profusion of rocks occurs in the ejecta surrounding the young impact crater shown in Figure 1. This crater is only 400 m in diam, so it is too small to be detected as an infrared anomaly or a 70-cm radar enhancement. This crater is detected but not resolved in the 3.8-cm radar maps. Rocky ejecta also surrounds another young crater shown in the Surveyor 1 photograph of Figure 2. We believe that the craters shown in Figures 1 and 2 are smaller versions of the types of craters detected as infrared and radar anomalies. The radar aboard the Surveyor 1 spacecraft showed an enhanced echo when the radar beam crossed young craters which were surrounded by blocky ejecta (Muhleman *et al.*, 1968).

The effects of aging on rocks are shown in Figure 3, two photographs taken by Apollo 12 astronauts. The fresh, angular blocks (Figure 3a) would be detected as an infrared and radar anomaly if these rocks occupied a large enough area to be detected. In contrast, the older rock shown in Figure 3b is much more pitted and much less angular. A large number of these rocks distributed over a large enough area would also be detected as an infrared and radar anomaly. But the concentration of older rocks would probably be a weaker anomaly than a similar concentration of fresh angular rocks.

3. Infrared and Radar Behavior Predicted by the Geologic Model

The previous review indicated that erosional processes will reduce the size and number of rocks associated with craters. In this section we will study the expected combinations of infrared and radar behavior during the aging of a lunar crater, based on the responses of the infrared and radar sensors as described above (see Sections 2A and 2B). For an overall view, Figure 4 shows the qualitative responses of these sensors to various rock sizes. In addition, Figure 4 shows how these responses will be modified as the rocks are buried at various depths in a fine-grained soil. The figure is a qualitative picture of the effects of rocks on the remote-sensed data. The 'relative response' scale may be thought of as the brightness of the IR or radar photomaps, where a fixed percentage area of the finely divided soil surface appears to be covered by rocks of the indicated size, under a soil layer of the indicated depth. In the case of the radar maps, a volume distribution of the same number of rocks is also possible if allowance is made for the electromagnetic attenuation through the soil material.

The lunar regolith layer becomes deeper and more fine grained with increasing age. However, some surface rocks will always be present ,as shallow cratering will exhume buried rocks from within the regolith and deep cratering will produce new rock fragments from the underlying bedrock and from shock lithification. Occasionally, very large impact events will excavate so much bedrock that the ejecta in the immediate vicinity of the crater will constitute a strewn field of rock fragments ranging in sizes up to several tens of meters. In time, this excess population of rocks will disappear.

Before considering the anomalous infrared and radar behavior, the average behavior of the Moon will be considered. Aside from small differences between mare and highlands, more than 90% of the lunar surface has remarkably similar behavior in the

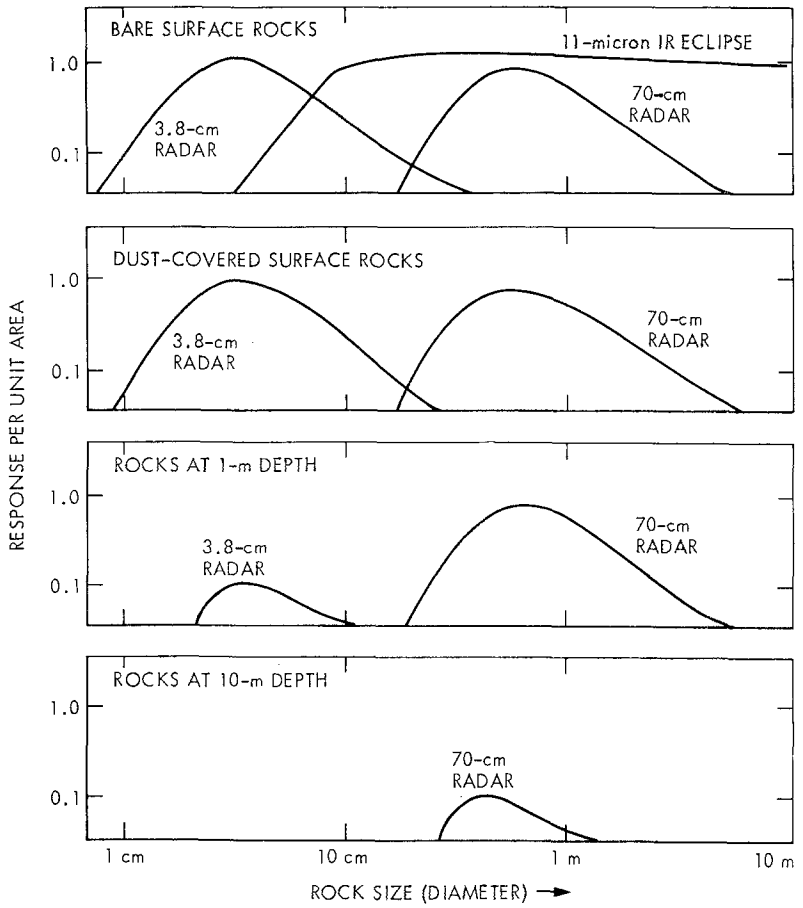

Fig. 4. Representative infrared and radar responses for lunar rocks with various burial conditions. These curves show the qualitative response of a unit area of lunar surface when a fixed small percentage of surface is covered by rocks of the indicated size. Horizontal and vertical scales are logarithmic. Our study indicates that dust covered rocks are improbable.

infrared and radar measurements. This 'average' behavior of the surface is typified by the fragmental debris layer observed at the Apollo landing sites and all Surveyor sites except Surveyor 7. For example, radar measurements indicate that the average lunar surface has a relative dielectric constant near 3 (Hagfors, 1970), which is consistent with a rock dust (Campbell and Ulrichs, 1969). Also, rocks observed on and near the surface probably cause the observed average background of depolarized radar scatter (Thompson *et al.*, 1970).

At infrared wavelengths, the average behavior of the surface is consistent with a porous dust. During the penumbral phase of an eclipse, the average surface cools rapidly with a temperature drop of 200 K in the first hour. Then, during the first hour of totality the temperature drop is only 10 K. A measure of the thermal properties of the lunar surface is the thermal parameter (the inverse of the thermal inertia) $\gamma = (k\varrho C)^{-1/2}$,

TABLE II

Surface conditions inferred from infrared and radar observations

Anomaly type	Infrared hot spot (enhanced eclipse temperature)	3.8-cm radar enhancement	70-cm radar enhancement	Inferred surface	Relationship to simplified geologic aging model discussed in Section 3	Occurrence
0	No	No	No	Normal distribution of rocks, old undisturbed surface	Asymptotic surface, provides basis for definition of anomalies; widespread	Most common
I	Yes	Yes	Yes	Excess number of centimeter- and meter-sized rocks	Predicted for recent cratering event	Common
II	Yes	Yes	No	Excess number of centimeter-sized rocks only: a very young and probably small feature	Behavior not predicted	Common
III	No	No	Yes	Older crater covered with a few meters of regolith	Predicted for cratering event of moderate age	Common
IV	Yes	No	Yes	Excess number of meter-sized surface rocks	Behavior not predicted	Rare
V	Yes	No	No	Excess number of smooth surface rocks much larger than meter-size, or smooth bare rock surface	Behavior not predicted	Rare
VI	No	Yes	Yes	Upper layer of regolith rough on centimeter and meter scale but no excess of bare surface rocks	Behavior not predicted	Rare
VII	No	Yes	No	Upper layer top of regolith rocky on centimeter scale but no excess of bare surface rocks; possibly, an excess number of surface rocks in 1–5-cm size range	Behavior not predicted	Rare

where k is the thermal conductivity, ϱ is the density, and C is the specific heat. Analysis of eclipse cooling indicates that the lunar surface has a γ of 1000 to 1300, but nighttime cooling indicates a γ of 800. This apparent contradiction was resolved by Winter and Saari (1969), who developed a particulate soil model for eclipse and nighttime cooling. This model consists of an array of opaque and approximately isothermal cubes. These cubes are in contact only along their edges; thus the porosity is one-half.

Here we are concerned more with departures from average behavior than with the average itself. If we characterized each area of the lunar surface as having a below average, average, or above average behavior in either eclipse temperature at 11 μ or radar backscatter at 3.8 and 70 cm, there would be 27 possible combinations of behavior among the three maps. However, areas with depressed temperatures or depressed radar backscatter response are less common and larger in size than areas with enhanced response. Thus we shall consider areas as being either average or anomalous according to our previous definitions (increased eclipse temperature or radar backscatter). This defines eight possible combinations of behavior, which are listed in Table II. The first entry in this table is called a type 0 anomaly and represents the average surface, which has no infrared or radar anomaly. Succeeding combinations or anomalies are called types I through VII. For each of these eight combinations, Table II lists the following items: the infrared and radar behaviors, our estimate of the inferred surface with the geologic model of the inferred surface, and our estimate of the frequency with which this combination occurs.

A. THE COMMON ANOMALIES, TYPES I, II, AND III

Anomaly types I, II, and III were encountered often. The type I anomaly, an infrared hot spot with a radar enhancement at 3.8 and 70 cm, appears most frequently. This is consistent with the model, since a cratering event karge enough to create a stewn field over many square kilometers should produce an excess of both centimeter- and meter-sized ejecta.

The type II anomaly is a definite hot spot and 3.8-cm radar enhancement with little no 70-cm radar enhancement. This combination of behaviors was unexpected on the basis of our model, since the infrared hot spot indicates an excess of surface rocks, yet the radar behavior indicates that surface rocks are predominately less that meter size. However, this type of anomaly occurs often; and, as mentioned before, we believe this is a distinct class of lunar feature. It must be young since meteoritic erosion will cause smaller rocks to disappear in a short time.

The type III anomaly is a definite 70-cm radar enhancement with near-average thermal and 3.8-cm radar behaviors. This type of anomaly would be expected for a crater which was originally a type of I anomaly but is now old enough to be covered with 0.5 to 5 m of regolith. This regolith is thick enough to give an average response for the 3.8-cm radar and infrared measurements but not thick enough to mask the diffuse scattering of buried meter-sized rocks. However, the 70-cm radar enhancement will be diminished.

B. THE RARE ANOMALIES, TYPES IV, V, VI, AND VII

Nearly all of the lunar surface has combinations of behavior described as anomaly types 0, I, II, and III (Zisk *et al.*, 1971; Shorthill *et al.*, 1972; Zisk *et al.*, 1972). The rare anomaly types (IV, V, VI, and VII) are either infrared hot spots or 3.8-cm radar enhancement, but not both. Thus the observations indicate that the infrared and 3.8-cm radar have similar behavior regardless of the 70-cm radar behavior. This is not surprising. An infrared hot spots results from an excess of surface rocks, which would appear at least as a 3.8-cm radar enhancement. Also, a 3.8-cm enhancement implies an excess of centimeter-sized rocks lying on the surface or buried no deeper than a meter. An excess of surface rocks is rejected, since they would appear as an infrared anomaly. The alternative surface condition required buried rocks, but these buried rocks would be quickly exhumed by cratering.

Because of their rarity, anomaly types IV, V, VI, and VII are extremely interesting features. Thus surface properties implied by these combinations of behavior are reviewed in the following paragraphs.

The type IV anomaly, an infrared anomaly with a 70-cm radar enhancement and average 3.8-cm radar backscattering, indicates an excess of surface rocks greater than a quarter-meter in size. It is doubtful whether a single natural event would selectively create an excess of only large rocks. However, this type of anomaly might be a crater which was originally a type I anomaly but which has aged so that small rocks have disappeared and larger rocks are left. This condition suggests that nearly all rocks would be eroded by impacts of particles very much smaller than centimeter size. Any large rock impacted by a particle smaller than centimeter size will be pitted on the centimeter scale. Furthermore, the spallation of the large rock would create centimeter-sized fragments. Thus we feel that this disruption by larger-particle bombardment is at least as important as erosion by small-particle bombardment in the destruction of lunar rocks.

The type Vanomaly, an infrared hot spot with no radar enhancements, indicates a large area of bare rock surface which is smooth on both the centimeter and meter scale. We consider this unlikely for the reasons outlined in the previous paragraph. That is, impacts of centimeter- and meter-sized particles would create centimeter- and meter-sized pits in the bare rock and would spall centimeter- and meter-sized fragments. Both the pits and fragments would cause radar enhancements.

The type VI and VII anomalies have radar enhancements with average thermal behavior, the expected response of dust-covered rocks. However, rocks observed at the Apollo and Surveyor landing sites were not dusty. Radar enhancements with no infrared anomaly could also result from an average distribution of surface rocks in a regolith which is rough on the centimeter or meter scale. This special surface would probably be destroyed by meteoritic bombardment. Another special surface condition, a scaled-down version of the type II anomaly, could create a type VI anomaly – a 3.8-cm radar enhancement with no infrared anomaly and no 70-cm radar enhancement. This requires ejecta in the size range of 3.8-cm radar enhancement yet small

enough to remain in thermal equilibrium with the lunar surface during an eclipse.

In summary, we have considered the eight possible combinations of average or anomalous behavior for eclipse temperatures at 11 μ and radar backscatter at 3.8- and 70-cm wavelength. These combinations, which are listed in Table II, are called anomaly types 0 through VII. Anomaly type 0 typifies the average surface, which has behavior consistent with regolith of lunar soil observed at the Surveyor and Apollo landing sites. Two common anomalies, type I and III, are younger and older versions of large cratering events which have modified many square kilometers of lunar surface. The type II anomaly is also common, but was considered unlikely in our prediction of the lunar surface conditions. We predicted that anomaly types IV, V, VI, and VII indicate improbable surface conditions, and, indeed, they are rarely observed. This implies that spallation of larger rocks by larger meteoritic particles occurs at least as often as the erosion of rocks by micrometeorites and that dust covered rocks do not form a significant portion of surface rock populations.

4. Behavior of 52 Craters

In the previous section, we hypothesized that the infrared and radar behavior of a crater is related to its geologic age. Of the 1000 to 2000 anomalies that appear in the infrared and radar maps, 52 craters were studied, chosen primarily from lists published in earlier reports of the most obvious infrared and radar enhancements.

Table III presents the 30 most prominent infrared anomalies reported by Shorthill and Saari (1965). The 18 features in Table IV were reported to be bright, diffuse areas in a 3.8-cm radar mapping of the Moon's equatorial belt (Lincoln Laboratory, 1968). (One crater, Messier A, appears in both of these lists.) Since the 47 craters given in Tables III and IV are young, we searched for anomalies associated with older craters. Although several examples were found, we will report on only four (Table V). In our search, we also discovered that the crater Encke had an unusual combination of infrared and radar behavior. In addition, a few craters from lists of prominent hot spots and bright, diffuse areas in the 3.8-cm maps also had unusual combinations of behavior. All craters with the unusual combinations of behavior are listed in Table VI. Each table is discussed separately below; the position of the selected craters, shown in Figure 5, is a near-global distribution.

The infrared and radar behavior for each crater in Tables III through VI is indicated by a three-digit enhancement number. The first digit gives the infrared behavior, the second digit gives the 3.8-cm radar behavior, and the third digit gives the 70-cm radar behavior. Since anomaly temperatures or backscatter vary by 2 orders of magnitude, the digits of the enhancement number were chosen by the logarithmic criteria listed in Table VII. Using this system, digits near 2 represent near-average behavior, while numbers of 6 or 7 are strong anomalies. In addition to the enhancement number, Tables III through VI give the full-Moon appearance, crater diameter, and the diameter of the 3.8-cm radar image. (In general, the halos seen in the 3.8-cm radar are not resolved in the infrared and 70-cm images). Also, geologic age is given in Table III.

TABLE III

Infrared, radar, and geologic characteristics of the 30 most prominent infrared hot spots

Crater[a]	Ranking[b]	Infrared/radar enhancement number[c]	Full Moon appearance (visual)	Geologic age	Crater diam (km)	3.8-cm radar image diam (km)[d]	Longitude (deg)	Latitude (deg)	Crater number Figure 5
Bode A	(29)	644	Bright interior	Copernican	12.3	40	1.2W	9.0N	1
Buch B	(4)	664	Bright interior	Copernican (post-Tycho)	6.7	40	17.0E	37.9S	2
Carlini	(3)	665	Bright interior	Copernican	11.4	–	24.1W	33.7N	3
Carlini D	(23)	655	Bright interior	Middle Copernican	9.3	–	16.0W	33.0N	4
Cauchy	(21)	566	Bright ray	Late Copernican	12.3	–	38.7E	9.6N	5
Cepheus A	(26)	646	Rays and halo	Late Copernican	12.5	–	46.5E	41.0N	6
Draper C	(7)	655	Bright interior	Copernican impact	7.7	–	21.5.5W	17.1N	7
EgedeA	(16)	665	Rays and halo	Late Copernican	12.5	25	10.5E	51.5E	8
Eudoxus A	(24)	646	Rays and halo	Late Copernican	14.1	60	20.1E	45.9N	9
Flamsteed B	(12)	644	Degraded halo	Copernican	9.4	–	43.7W	5.9S	10
Gambart C	(22)	634	Bright interior	Early Copernican	12.2	–	11.8W	3.3N	11
Guericke C	(11)	65N	Ray and halo	Late Copernican	10.9	Ray	11.5W	11.6S	12
Hesiodus B	(27)	556	Bright interior	Early Copernican, Late Eratosthenian	10.2	–	17.5W	27.9S	13
Jansen E	(5)	664	Bright halo	Copernican	7.0	–	27.8E	17.5N	14
Jansen F	(14)	665	Halo and rays	Copernican	9.4	Ray	31.0E	12.6N	15
Janssen K	(28)	676	Halo and rays	Copernican	15.5	50	42.2E	46.2S	16
Laplace A	(17)	(17)	Halo and rays	Late Copernican	9.7	–	29.9W	43.7N	17
Maraldi B	(8)	655	Bright interior, Faint ray and halo	Early Copernican/ Late Erathosthenian	74	–	36.8E	14.4N	18
Marius A	(15)	745	Bright interior	Middle Copernican	16.0	–	46.0W	12.6N	19

[a] Crater Messier A listed in both Tables III and IV.
[b] Ranking = listing in order of prominence after a real correction (Shorthill and Saari, 1965).
[c] N in enhancement number = 70-cm data (craters Guericke C, Mösting A, and Mösting C);
[d] R in enhancement number = 3.8-cm radar enhancement only on rim (crater Nicollet).
[e] Ray in 3.8-cm radar image diameter = indication of rays in 3.8-cm image (craters Guericke C and Jansen F);
[f] Dash = no indication of radar halo or rays.

Table III (continued)

Crater[a]	Ranking[b]	Infrared/radar enhancement number[c]	Full Moon appearance (visual)	Geologic age	Crater diam (km)	3.8-cm radar image diam (km)[d]	Longitude (deg)	Latitude (deg)	Crater number Figure 5
Mason C	(20)	665	Bright interior	Early Copernican	12.3	–	33.8E	42.9N	20
Messier A	(3)	674	Halo and rays	Late Copernican	13.8	30	46.9E	2.0S	21/46
Moltke	(9)	542	Halo and rays	Late Copernican	6.4	25	24.2E	0.6S	22
Mösting A	(19)	57N	Halo and rays	Copernican	13.0	30	5.3W	3.2S	23
Mösting C	(1)	57N	Halo and rays	Copernican	3.8	30	8.1W	1.8S	24
Nicollet	(18)	6R4	Bright rim Dark floor	Eratosthenian or may be volcanic	15.2	–	12.5W	21.9S	25
Pico B	(25)	645	Bright rim Faint floor	Eratosthenian	11.4	–	15.3W	46.4N	26
Piton B	(2)	564	Bright interior	Late Copernican	4.8	50	0.2W	39.3N	27
Plato M	(10)	655	Halo, no rays	Copernican	8.3	20	15.5W	53.0N	28
Taruntius H	(13)	653	Bright interior	Eratosthenian	6.9	–	49.8E	0.4N	29
Torricelli B	(6)	624	Bright interior	Eratosthenian	6.9	–	29.2E	2.6S	30

[a] Crater Messier A listed in both Tables III and IV.
[b] Ranking = listing in order of prominence after areal correction (Shorthill and Saari, 1965).
[c] N in enhancement number = 70-cm data (craters Guericke C, Mösting A, and Mösting C);
[d] R in enhancement number = 3.8-cm radar enhancement only on rim (crater Nicollet).
[e] Ray in 3.8-cm radar image diameter = indication of rays in 3.8-cm image (craters Guericke C and Jansen F);
[f] Dash = no indication of radar halo or rays.

TABLE IV

Infrared, radar, and visual characteristics of 18 diffuse areas in the 3.8-cm radar maps

Feature[a]	Infrared/radar enhancement number[b]	Full Moon appearance	Crater diam (km)[c]	3.8-cm image diam (km)[c]	Longitude (deg)	Latitude (deg)	Crater number: Figure 5
Rocca Ab	563	Bright halo	10	30	68.4W	12.7S	31
Near Rocca Fa	264	Bright halo	4	15	66.7W	14.5S	32
Grimaldi G	564	Halo and rays	12	25	64.8W	7.8S	33
Siralis J	43C	Bright interior	12	15	59.7W	13.4S	34
Flamsteed Gc	663	Halo and rays	5	25	52.5W	3.2S	35
Unnamed Crater	563	Small bright spot	4	15	50.3W	0.2S	36
Suess	663	Bright interior	9	25	47.9W	4.0N	37
Gassendi F	565	Bright halo	5	30	45.2W	14.9S	38
Cluster of small craters	594	Bright halo	–	40	42.3W	7.2N	39
Encke X	633	Bright halo	4	70	40.2W	1.0N	40
Herigonius Ec	644	Bright halo	4	40	36.4W	12.8S	41
Reinhold Na	264	No brightening	2	25	25.7W	1.9N	42
Censorinus	67P	Bright halo and rays	4	60	32.7E	0.4S	43
Two craters between Capella C, and CA	574	Bright halo	–	20	36.2E	6.1S	44
Secchi A	544	Bright interior	5	15	41.2S	3.3N	45
Messier A[b]	674	Halo and rays	14	30	46.9E	2.0S	46/21
Taruntius K	542	Bright interior	3	50	51.5E	0.7N	47
Small crater on east rim of Lick	362	Bright halo	2	20	53.3E	12.4N	48

[a] From Lincoln Laboratory, 1968.
[b] Crater Messier A listed in both Tables III and IV.
[c] C in Enhancement Number = Confused by adjacent enhancements (crater Siralis J).
[d] P in Enhancement Number = Poor quality data (crater Censorinus).
[e] No crater diameter listed for diffuse areas associated with more than one crater.

TABLE V

Infrared, radar, and visual characteristics of four older craters

Crater	Infrared/radar enhancement number[a]	Full Moon appearance[b]	Crater diam (km)	Longitude (deg)	Latitude (deg)	Crater number: Figure 5
Descartes A	355	Bright rim; moderately bright floor	15.4	15.2E	12.1S	49
Gassendi	334	Dark floor; bright rim	110.4	39.8W	17.5S	50
Kant	324	Bright rim; bright peak; dark floor	31.7	20.2E	10.6S	51
Reinhold	224	No brightening	47.5	22.8W	3.3N	52

[a] 3.8-cm enhancement indicates radar behavior of floor.

[b] All craters had brighter rims than floors in 3.8-cm radar images; crater Kant had bright central peak; floor of Gassendi has several lesser bright spots.

TABLE VI

Infrared, radar, and visual characteristics of craters with unusual combinations of infrared and radar behaviors

Crater	Infrared/radar enhancement number[a]	Anomaly type[b]	Full Moon appearance	Crater diam (km)	Longitude (deg)	Latitude (deg)	Crater number: Figure 1
Encke	344	VI	Bright rim/ slightly bright	29.4	36.6W	2.3N	53
Gambart C	634	IV	Bright interior/ no rays	12.2	11.8W	3.3N	11
Nicollet	6R4	IV	Bright rim/ dark floor	15.2	12.5W	21.9S	25
Torricelli B	624	IV	Bright interior/ no rays	6.9	29.2E	2.6S	30
Near Rocca Fa	264	VI	Bright halo	4	66.7W	14.5S	32
Reinhold Na	264	VI	No brightening	2	25.7W	1.9N	42
Encke X	633	V	Bright halo	4	40.2W	1.0N	40
East rim of Lick	362	VII	Bright halo	2	53.3E	12.4N	48

[a] R in radar enhancement number = rim only enhancement (Nicollet).

[b] See Table II.

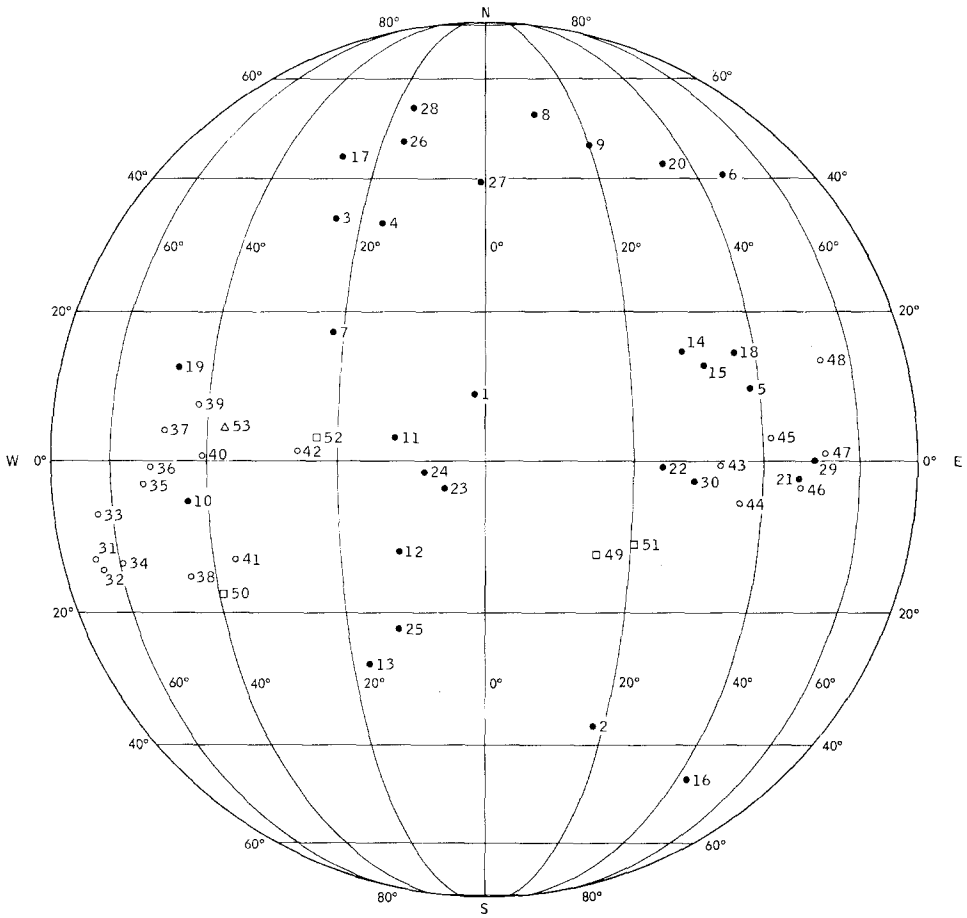

Fig. 5. Location of the 52 lunar craters selected for study. Solid circles are prominent infrared anomalies; open circles are bright, diffuse areas in 3.8-cm radar map; squares are older craters; triangles are craters showing unexpected infrared and radar behaviors. Crater Messier A (21 and 46) occurred on two different lists. Note the near-global distribution of these craters.

A. TABLE III: THIRTY PROMINENT INFRARED ANOMALIES

The 30 craters were chosen for study because they were the strongest infrared anomalies after being areally corrected (Shorthill and Saari, 1965). The infrared behavior indicates that these craters have an excess of exposed rocks greater than 10 cm in size. The rocks would be expected to create an increased radar backscatter. An excess of rocks from 1 to 40 cm in size would create a 3.8-cm enhancement; an excess of rocks from 20 cm to 7 m in size would create a 70-cm radar enhancement.

With reference to the crater againg model inferred from geologic studies, the strong infrared anomalies should be young craters with strewn fields of rocks. These craters should have sharp rims, hummocky ejecta, a bright appearance, and prominent rays. Table III shows that these conditions do exist for most of these craters

TABLE VII

Criteria for choosing the infrared/radar enhancement number

A, B, C[a]	A = thermal behavior[b]	B, C = radar behavior[c]
0	$-1 \leqslant \Delta FM < 0$	$0 \leqslant S < \frac{1}{4}$
1	$0 \leqslant \Delta FM < 1$	$\frac{1}{4} \leqslant S < \frac{1}{2}$
2	$1 \leqslant \Delta FM < 2$	$\frac{1}{2} \leqslant S < 1$
3	$2 \leqslant \Delta FM < 4$	$1 \leqslant S < 2$
4	$4 \leqslant \Delta FM < 8$	$2 \leqslant S \quad 4$
5	$8 \leqslant \Delta FM < 16$	$4 \leqslant S < 8$
6	$16 \leqslant \Delta FM < 32$	$8 \leqslant S < 16$
7	$32 \leqslant \Delta FM$	$16 \leqslant S$

[a] Infrared/radar enhancement number = ABC
where A = indication of thermal behavior at 11μ
B = indication of 3.8-cm radar scattering
C = indication of 70-cm radar scattering

[b] FM = flattened Moon contour described in equation 1 ($\Delta FM = 1$ is nominal upland behavior).

[c] S = normalized radar cross-section for depolarized echoes ($S = 1$ is average over lunar disk for 3.8-cm map and average over a LAC chart for 70-cm map).

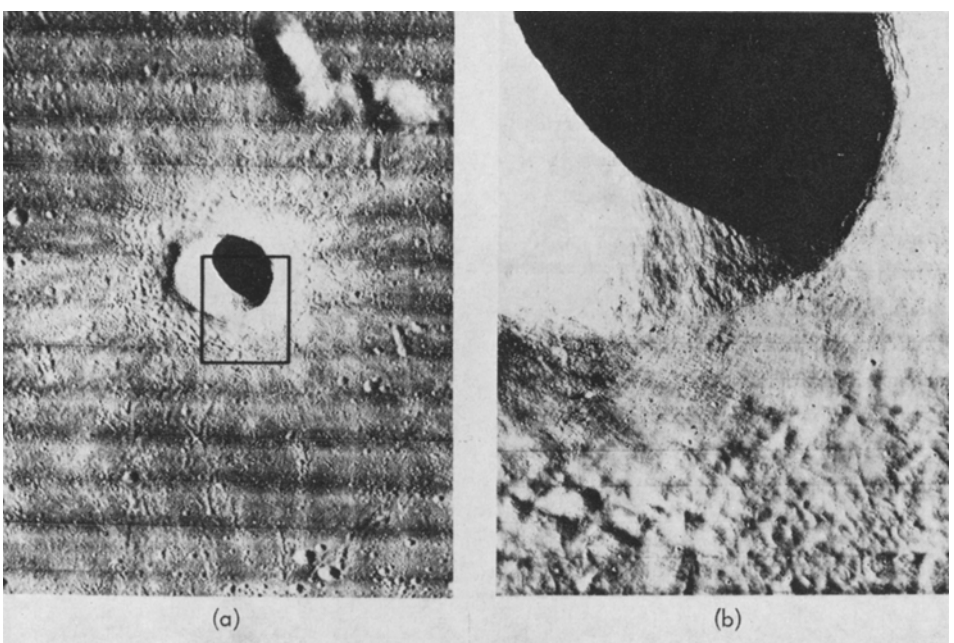

Fig. 6. (a) Crater Mösting C (3.8-km diam, 8.1°W, 8°S; Lunar Orbiter III photograph M-113). Mösting C is a young Copernican crater, probably one of the youngest craters on the Moon. It has hummocky ejects; large rocks are exposed on its rim. The 3.8-cm radar enhancement, which extends beyond the crater by 7 crater radii, encompasses all of the area shown in (a). (b) Some of the exposed rocks on the rim of crater Mösting C (Lunar Orbiter III photograph H-113)

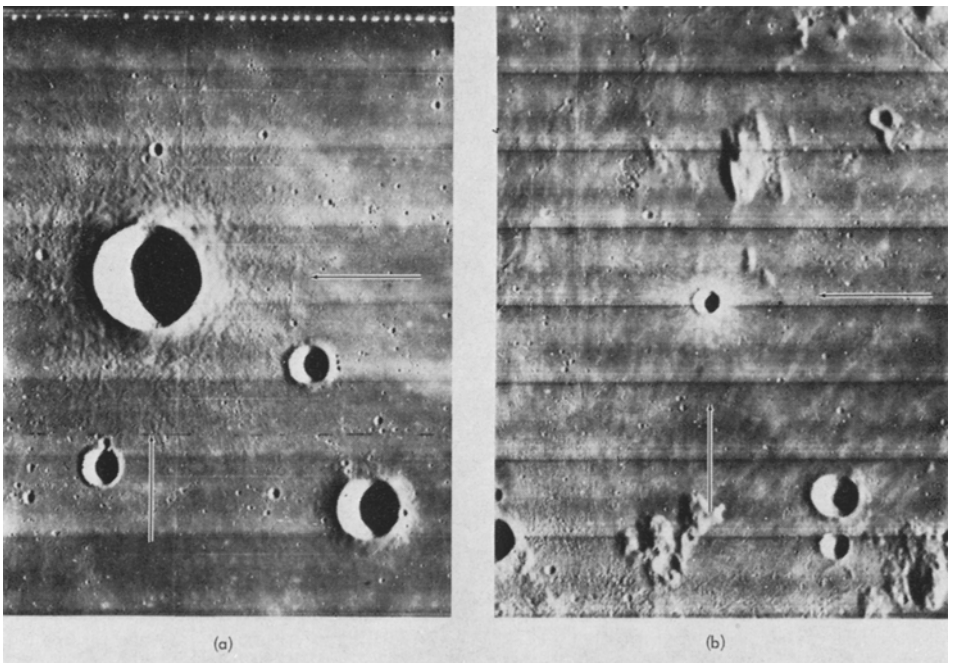

Fig. 7. (a) Crater Marius A (16.0-km diam, 46°W, 12.6°N; Lunar Orbiter IV photograph H-144). (b) Crater Mösting C (3.8-km diam, 8.1°W, 1.8°S, Lunar Orbiter IV photograph H-113). Mösting C is a young Copernican crater also shown in Figure 1. Marius A is a middle Copernican crater, having a more subdued ejecta blanket than Mösting C. Marius A has no rays. However, Marius A is a prominent infrared and radar anomaly.

with pronounced infrared anomalies. An example of a young crater of Copernican age is Mösting C (Figure 6 and 7b). The hummocky ejecta which surrounds this crater has enhanced 3.8-cm radar scatter. In fact, the 3.8-cm radar enhancement for this cater extends beyond the crater by 7 crater radii and encompasses all of the area of Figure 6a. Some of the exposed rocks associated with this crater are shown in the high-resolution photograph (Figure 6b).

Twenty-five of the prominent infrared anomalies are of Copernican age, although some of these 25 craters are noticeably older than Mösting C. Marius A (Figure 7a) is one example of a middle-Copernican crater. Both Mösting C and Marius A have sharp rims and hummocky ejecta; however, Mösting C has rays, whereas Marius A does not. Only five of the prominent infrared anomalies – Maraldi B, Hesiodus B, Pico B, Taruntius H, and Torricelli B – are as old as Eratosthenian. Two older craters, Maraldi B and Torricelli B, show only a slight 3.8-cm enhancement. Another interesting crater is Nicollet (Figure 8), which displays strong thermal and 70-cm radar enhancement. However, a 3.8-cm radar enhancement and full-Moon brightening occur only on its rim. Its subdued appearance and lack of an extended ejecta suggest that Nicollet may be a volcanic crater or an older (Eratosthenian) impact crater. One

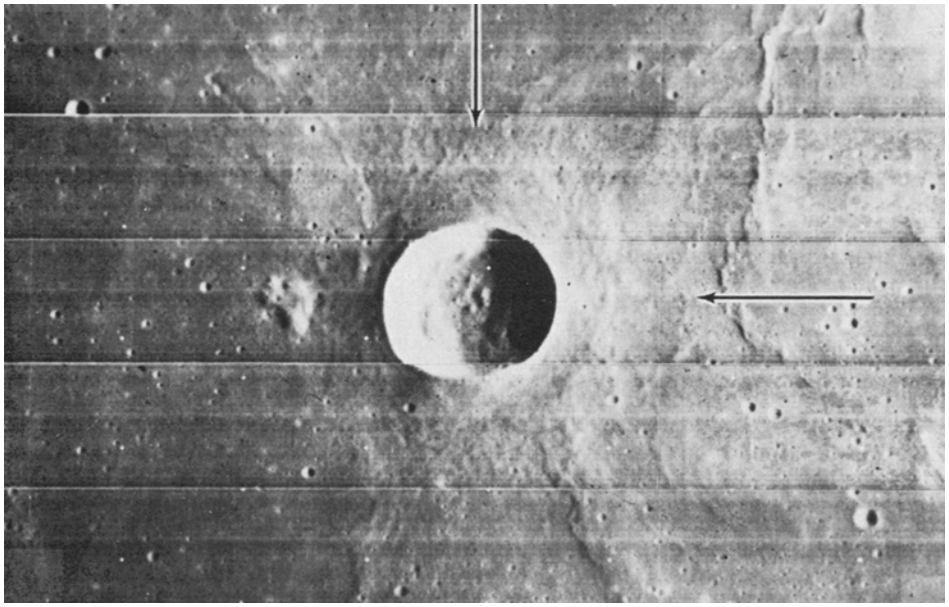

Fig. 8. Crater Nicollet (15.2-km diam, 12.4°W, 21.9°S, Lunar Orbiter IV photograph H-120). Nicollet is either a degraded Erastothenian impact crater or a volcanic crater of uncertain age. The floor is dark in full Moon illumination and has no 3.8-cm radar enhancement. The rim is bright and has a definite 3.8-cm radar enhancement. However, this crater is a strong infrared hot spot and 70-cm radar enhancement.

crater, Moltke, has no 70-cm radar enhancement, is a type II anomaly, and resembles the craters of Table IV.

B. TABLE IV: BRIGHT DIFFUSE AREAS IN 3.8-CM RADAR MAPS

In addition to the 30 prominent infrared anomalies, we studied 18 features which appear as bright, diffuse areas in the 3.8-cm radar maps. Most of these features are the type II anomalies, which were not predicted on our geologic model.

The 18 features in Table IV were reported in an earlier mapping of polarized echoes from the equatorial region (16°N to 16°S) of the Moon (Lincoln Laboratory, 1968). Since polarized echoes are not altered significantly by roughness within 25° of the subradar point, the anomalies in Table IV lie beyond 25° of longitude. However, later maps of depolarized echoes indicate that these bright, diffuse areas are common features throughout the earthside hemisphere. Particularly striking examples of the Type II anomalies are the crater Linné in Mare Serenitatis and the crater Hell QA on the floor of the larger, older crater Deslandres, southwest of Mare Nubium.

These bright, diffuse areas have several interesting properties. Most of them surround small, fresh-looking craters with diameters of only a few kilometers. Two of these areas are associated with clusters of craters whose individual diameters are only a few hundred meters. Nevertheless, all of the 3.8-cm radar enhancements are tens

of kilometers in diameter. Generally, the 3.8-cm radar enhancements are accompanied by infrared anomalies, which are probably fields of surface rocks. Also these areas generally have little or no 70-cm radar enhancement, indicating that the surface rocks are no more than a few tens of centimeters in size. It is surprising that a natural event created a strewn field several hundred square kilometers in area which is devoid of meter-sized rocks. As meteoritic bombardment erodes centimeter-sized rocks faster than meter-sized rocks, these areas must be young features. Therefore, it is not surprising that these features are visual bright spots during the full Moon.

Most of the features in Table IV are craters classed as type II anomalies – definite infrared and 3.8-cm radar anomalies but with little or no 70-cm radar enhancement.

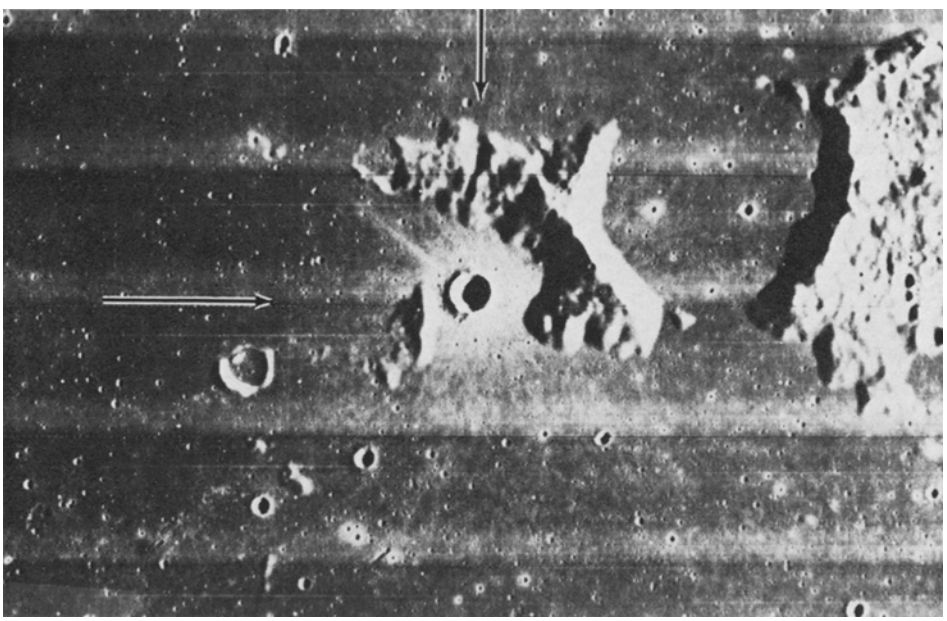

Fig. 9. Crater Flamsteed Gc (5.0-km diam, 52.5° W, 3.2° S, Lunar Orbiter IV photograph H-149). Flamsteed Gc is a typical Type II anomaly – an infrared hot spot and 3.8-cm radar enhancement with a 70-cm radar echo strength of only 1.5 times the average. The 3.8-cm radar enhancement extends to 5 crater radii beyond the crater. The rays, which are apparent even in the low-sun illumination of this picture, indicate that this is a very young feature.

A typical type II anomaly is the crater Flamsteed Gc (Figure 9). The bright rays, which appear even in the low Sun illumination of this photograph, indicate that Flamsteed Gc is very young.

However a few type II anomalies are not associated with a single crater. For example, the feature called 'cluster of small craters' in Table IV is the large, diffuse area about 40 km in diam, whose 3.8-cm (depolarized) radar image is shown in Figure 10a. At the level of exposure for the radar image, three bright nuclei are im-

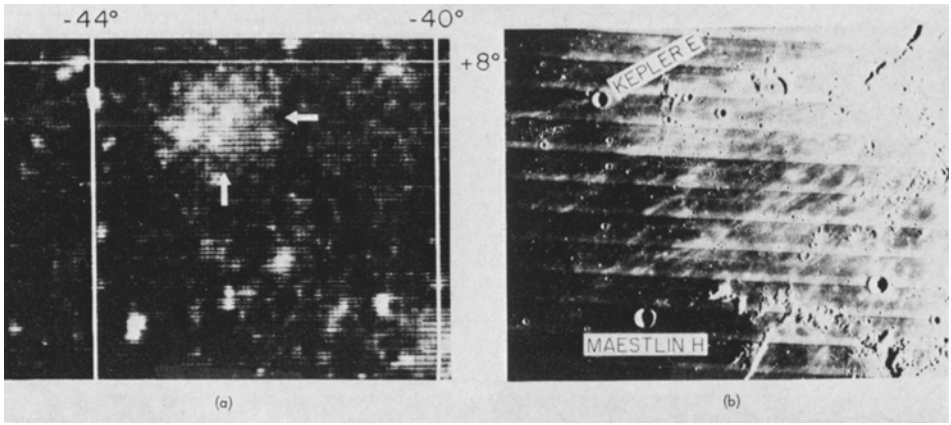

Fig.10. The 3.8-cm (depolarized) radar image (a), and Lunar Orbiter photograph (b) of an area in Oceanus Procellarum (west of crater Kepler) which has a 3.8-cm enhancement not associated with a crater. The 3.8-cm radar image is taken from map area ZAC 5.24 (Lincoln Laboratory, 1970) and is underexposed to show the nuclei in enhanced area. The photograph is Lunar Orbiter IV, H-144, and the framelet width is approx. 10 km. The diffuse, enhanced area in the radar map is called 'Cluster of Small Craters' in Table V, and is a type II anomaly (see Table II). However, two of the bright nuclei of the 3.8-cm radar enhanced areas are not associated with sizeable craters (diam. greater than 1 km).

bedded in the enhanced area. Only one of these nuclei is identified with a crater – the eastermost 3-km crater shown in Figure 10b. The other two nuclei may be centered on the smaller craters in the enhanced area, but no identification is possible.

A few craters in Table IV are not type II anomalies. For example, Reinhold NA and a crater near Rocca Fa have no thermal anomaly but do display significant radar enhancements at both 3.8- and 70-cm wavelengths. Furthermore, Reinhold NA does not show any brightening during the full Moon. Another crater, Encke X, shows a strong thermal anomaly but only slightly enhanced radar scattering at both 3.8 and 70 cm. Also, an unnamed crater located on the east rim of Lick shows an extremely strong 3.8-cm enhancement, no radar enhancement at 70-cm, and only a weak infrared anomaly.

C. TABLE V: OLDER CRATERS

In addition to the young craters listed in the preceding tables, four older craters (Table V) were studied. One crater, Descartes A, has characteristics of an intermediate age crater. Its rim is clearly enhanced in 3.8-cm return, but its floor is only moderately enhanced. Radar characteristics for all these older craters are similar to the full Moon albedo in that the rims are bright whereas the floors have average values. The other craters in Table V – Gassendi, Kant, and Reinhold – are probably older than Descartes A because their floors have near average scattering values at 3.8 cm. However, each has a bright rim at the same wavelength and a definitely enhanced rim and floor at 70-cm wavelengths. Thus Gassendi, Kant, and Reinhold are type III anomalies.

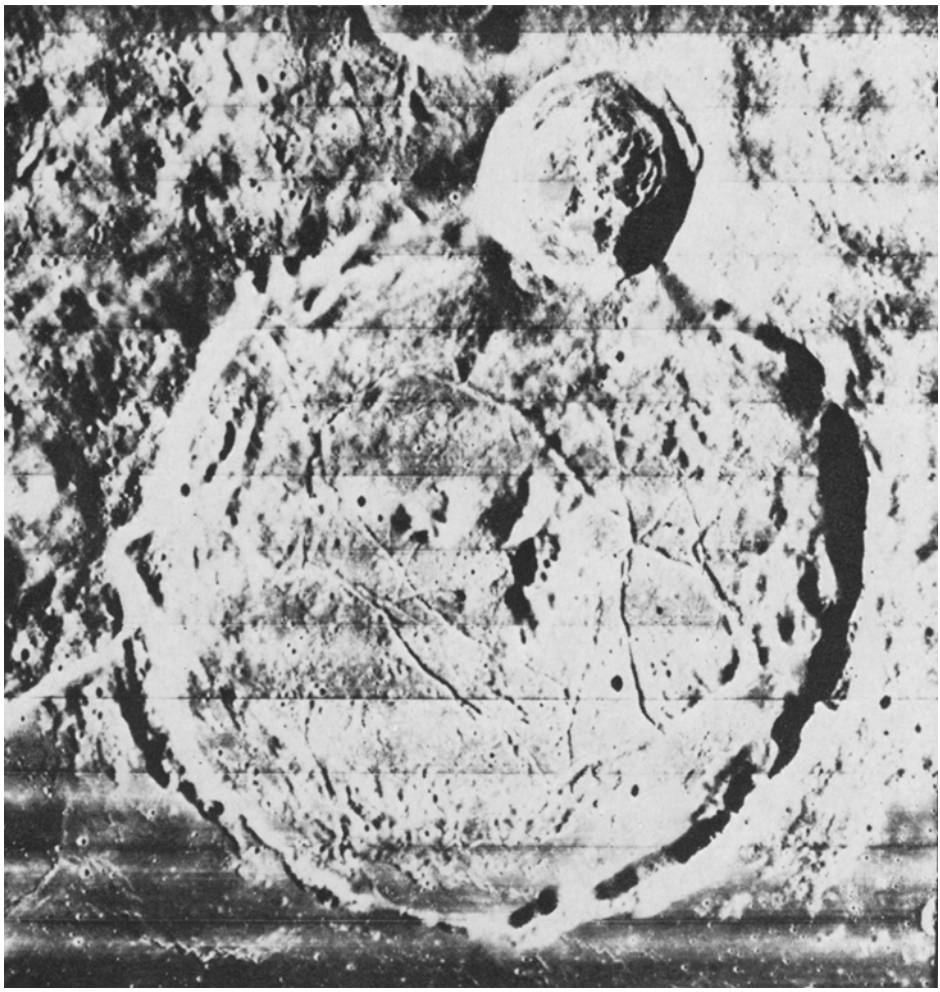

Fig. 11. Crater Gassendi (110-km diam, 39.8° W, 17.5° S, Lunar Orbiter IV photograph H-143). Gassendi is a type III anomaly – a definite (2:1) 70-cm radar enhancement with no infrared anomaly and no 3.8-cm radar enhancement. The presence of mare material at the southern rim of Gassendi dates this crater as pre-mare (Imbrian). In contrast, the younger Gassendi A on the northern rim of Gassendi is a type I anomaly – definite infrared hot spot having pronounced 3.8- and 70-cm radar enhancements.

Gassendi (Figure 11), which is partly flooded by mare material, is Imbrian in age and therefore older than the other craters in Tables IV and V.

D. TABLE VI: UNEXPECTED INFRARED AND RADAR BEHAVIOR

Table VI lists the craters with unexpected combinations of infrared and radar behaviors – anomaly types IV through VII. Several of these craters are found in Tables IV and V and are described above. Also, crater Encke has definite (2:1) radar enhance-

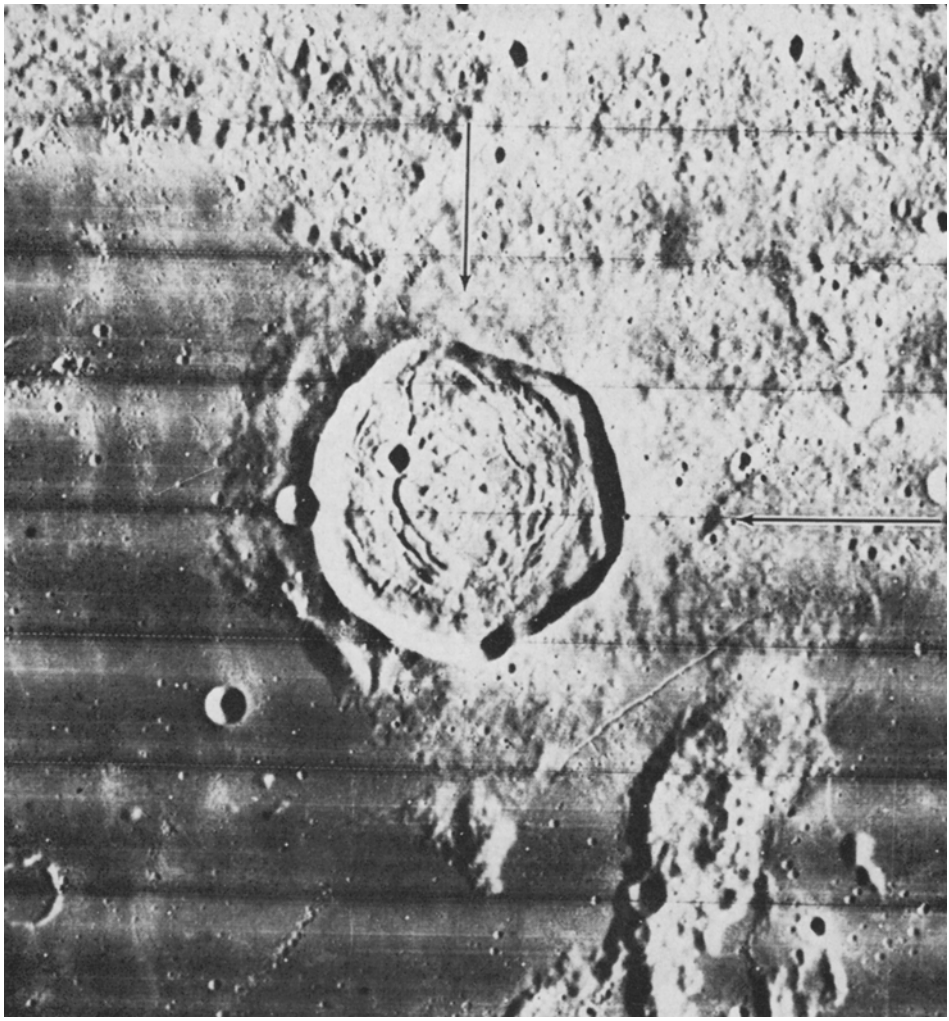

Fig. 12. Crater Encke (16.9-km diam, 36.6°W, 2.3°N, Lunar Orbiter IV photograph H-138). Encke has the unexpected combination of a pronounced 3.8- and 70-cm radar enhancements but no thermal anomaly. This crater may be a volcanic caldera.

ment at both 3.8- and 70-cm wavelengths but no infrared anomaly. This crater, which is shown in Figure 12, appears to be one of the few examples of volcanic caldera on the Moon. Regardless of its origin, it does have a special combination of surface properties.

5. Summary and Concluding Remarks

This study relates the radar and infrared responses of the lunar surface to geologic inferences based on analyses of visual images. We have assumed that the lunar

surface consists of regolith – a layer of fragmental debris overlying a coherent bedrock. Furthermore, we have assumed that most infrared and radar anomalies result from excess rock populations caused by large cratering events which have penetrated the regolith and excavated large quantities of bedrock and redeposited these rocks in strew fields which are many kilometers across.

These rock fields are modified with time by meteoritic bombardment which grinds them into the fine-grained debris observed at the lunar landing sites. The data presented for the prominent infrared anomalies (Table III) indicate that these strewn fields are young features; most are Copernican in age but a few are Eratosthenian. Nearly all of the Eratosthenian craters have definite 3.8-cm radar enhancements, indicating that centimeter-sized rocks and roughness are still present. Thus, spallation of rocks by impacts with enough energy to fracture centimeter-sized and larger rocks is common lunar process. The aging of older craters is expected to create a debris layer shallow enough to be penetrated by radar waves of meter wavelengths but deep enough to be average or near average at infrared and centimeter-radar wavelengths. These anomalies are of late Imbrian or early Eratosthenian age. Also, the rims of these older craters tend to remain anomalous while the floors tend toward average behavior.

Besides these anomalies, which are consistent with our model, another type of lunar feature is quite common. These areas are bright in the 3.8-cm radar maps, are infrared hot spots, but have only average radar scattering at 70-cm. The combination of the infrared and radar behaviors indicates that these areas are strewn fields of predominantly centimeter-sized fragments. These strewn fields are often tens of kilometers in diameter surrounding a crater whose diameter is only few kilometers. Since the ejecta is primarily centimeter-sized, these must be young features. However, it is surprising that these events do not produce an excess of meter-sized rocks.

A few other craters have behaviors which indicate surface conditions not predicted by our model. However, the infrared, radar, and geologic maps do complement each other and, for the most part, these maps are consistent with our present understanding of lunar surface processes.

Acknowledgements

The authors wish to thank the following people for their assistance during this study: Donald E. Gault of Ames Research Laboratory and Gerald G. Schaber and George Colton of the United States Geological Survey, who suggested many important changes in the text, James Sasser of the Manned Spaceflight Center, who provided Lunar Orbiter photographs, and G. K. Bruce of the Boeing Scientific Research Laboratories, for transferring flattened Moon contours to the LAC base.

Geological mapping by the United States Geological Survey was done under NASA Contracts W-12388 and T-94142. The flattened Moon contours produced in the infrared mapping were done under NASA Contract NAS 9-9794 (Manned Spacecraft Center, Houston, Texas). The 3.8-cm radar mapping studies were carried out with financial assistance from NASA under Contract NAS 9-7830. The use of

the Haystack radar and other support facilities of MIT Lincoln Laboratory is gratefully acknowledged. The 70-cm radar mapping studies were sponsored in part by NASA Grant 33-010-024 and in part by the continuing grants to the Arecibo Observatory by the National Science Foundation and the Advanced Research Projects Agency (Air Force Office of Scientific Research).

The work performed by T. W. Thompson at the Jet Propulsion Laboratory was sponsored by the National Aeronautics and Space Administration under Contract No. NAS 7-100-55, and by Apollo Experiment S-217, 'IR and Radar Study of Apollo Data'.

References

Allen, D. A.: 1971, *The Moon* **2**, 320–337.
Baldwin, R. B.: 1949, *The Face of the Moon*, University of Chicago Press, Chicago, Illinois.
Baldwin, R. B.: 1963, *The Measure of the Moon*, University of Chicago Press, Chicago, Illinois.
Burns, A. A.: 1969, *J. Geophys. Res.* **75**, 1467–1482.
Campbell, M. J. and Ulrichs, J.: 1969, *J. Geophys. Res.* **74**, 5867–5881.
Carr, M. H.: 1964, *Trajectories of the Objects Producing Copernican Ray Material on Eratosthenes*, U.S. Geol. Survey Open-File Report, Astrogeologic Studies Progress Report, Pt. A, pp. 33–41.
Dietz, R. S.: 1946, *J. Geology* **54** 359–375.
Dodd, R. T., Jr., Salisbury, J. W., and Smalley, V. C.: 1963, *Icarus* **2**, 466–480.
Gault, D. E.: 1970, *Radio Sci.* **5**, 273–291.
Gilbert, G. K.: 1893, *Philos. Soc. Washington Bull.* **12**, 241–292.
Guest, J. E. and Murray, J. B.: 1969, *Planetary Space Sci.* **17**, 121–141.
Hackman, R. J.: 1966, *Geologic Map of the Montes Apenninus Region of the Moon*: U.S. Geol. Survey Misc. Geol. Inv. Map I-463 (LAC-41).
Hagfors, T.: 1967, *Radio Sci.* **2**, 455–465.
Hagfors, T.: 1970, *Radio Sci.*, No. 2, 189–227.
Hartmann, W. K. and Kuiper, G. P.: 1962, *Arizona Univ. Lunar and Planetary Lab. Comm.* **1**, 51–66.
Keen, G. C.: 1965, *Lunar Orbiter Photo Study Z – 3841*, Eastman Kodak Company, Rochester, New York.
Khabakov, A. V.: 1949, 'Basic Aspects of the History of the Moon's Surface', *Zap. Vses. geogr. o-va*, Nov. Ser., 6.
Kosofsky, L. J. and El-Baz, F.: 1970, *The Moon as Viewed by Lunar Orbiter*, National Aeronautics and Space Adm., Spec. Pub. SP-200.
Kuiper, G. P.: 1965, 'Interpretation of Ranger VII Records', in *Ranger VII. Part 2: Experimenters' Analyses and Interpretations*, Technical Report 32-700, Pasadena, Calif., pp. 9–73.
Kuiper, G. P., Strom, R. G., and LePoole, R.: 1966, 'Interpretations of the Ranger Records', in *Ranger VIII and IX. Part II. Experimenters' Analyses and Interpretations*, Technical Report 32-800, Jet Propulsion Laboratory, Pasadena, Calif., 35–248.
Lincoln Laboratory: 1968, *Radar Studies of the Moon*, Final Report, Vol. 2, NSR 22-0009-106, Massachusetts Institute of Technology, Lexington, Massachusetts.
Lincoln Laboratory: 1970, *Radar Studies of the Moon: Vol. I; Radar Atlas of the Moon: Vols. II and III*, NAS 9-7830, Massachusetts Institute of Technology, Lexington, Massachusetts.
Low, F. J. and Mendell, W. N.: 'An Overview of Early Data From the Apollo 17 Infrared Scanning Radiometer', presented at the *Fourth Lunar Science Conf.* JSC, Houston, Texas, Mar. 5-8, 1973.
Masursky, H.: 1968, 'Preliminary Geologic Interpretations of Lunar Orbiter Photographs', *1969 NASA Authorization, 90th Congress H.R. 15086, No. 3*, pp. 664–691.
Masursky, H., Batson, R., and Borgeson, W.: 1970, *Icarus* **12**, 10–45.
McCauley, J. F.: 1967, in S. K. Runcorn (ed.), *Mantles of the Earth and Terrestrial Planets*, Interscience Press, New York, pp. 431–460.
Morris, E. C., Batson, R. M., Holt, H. E., Rennilson, J. J., Shoemaker, E. M., and Whitaker, E. A.: 1968, 'Television Observations from Surveyor VI', in *Surveyor VI Mission Report. Part II. Science Results*, Technical Report 32-1265, Jet Propulsion Laboratory, Pasadena, Calif.
Muhleman, D. O., Brown, W. E., Davids, L., and Peake, W. H.: 1968, 'Lunar Surface Electro-

magnetic Properties', Chapter VII in *Surveyor Project Final Report. Part II. Science Results*, Technical Report 32-1265, Jet Propulsion Laboratory, Pasadena, Calif.
Oberbeck, R. R. and Quaide, W. L.: 1968, *Icarus* **9**, 445–465.
Pettengill, G. H. and Thompson, T. W.: 1968, *Icarus* **8**, 457–471.
Pohn, H. A. and Offield, T. W.: 1970, 'Lunar Crater Morphology and Relative Age Determination of Lunar Geologic Units – Classification', in *Geological Survey Research 1970, U.S. Geol. Survey*, Prof. Paper 700-C, C153-C162.
Quaide, W. L. and Oberbeck, V. R.: 1969, *Earth-Sci. Rev.* **5**, 255–278.
Roelof, E. C.: 1968, *Icarus* **8**, 138–159.
Schmitt, H. H., Trask, N. J., and Shoemaker, E. M.: 1967, *Geologic Map of the Copernicus Quadrangle of the Moon*, U. S. Geol. Survey Misc. Geol. Inv. Map I-515 (LAC-58), 1967.
Shoemaker, E. M.: 1961, *Prototype Geologic Map of the Copernicus Region of the Moon*, U.S. Geol. Survey Open-File Report.
Shoemaker, E. M.: 1962, in Z. Kopal (ed.), *Physics and Astronomy of the Moon*, Academic Press, New York, pp. 283–359.
Shoemaker, E. M. and Hackmann, R. J.: 1962, in Z. Kopal and Z. K. Mikhailov (eds.), 'The Moon' *IAU Symp.* **14**, Academic Press, New York, pp. 298–300.
Shoemaker, E. M. and Morris, E. C.: 1970, *Radio Sci.* **5**, 129–155.
Shoemaker, E. M., Hait, M. H., Swann, G. A., Schleicher, D. L., Dahlem, D. H., Schaber, G. G., and Sutton, R. L.: 1970a, *Science* **167**, 452–455.
Shoemaker, E. M., Hait, M. H., Swann, G. A., Schleicher, D. L., Schaber, G. G., Sutton, R. L., Dahlem, D. H., Goddard, E. N., and Waters, A. C.: 1970b, *Proceedings of the Apollo 11 Lunar Sci. Conf., Geochem. Cosmochim. Acta* **3** (Supplement 1), 2399–2412.
Shorthill, R. W.: 1970, *J. Spacecraft and Rockets* **7**, 385–397.
Shorthill, R. W.: 1973, 'Infrared Atlas Charts of the Eclipsed Moon', *The Moon*, accepted for publication.
Shorthill, R. W. and Saari, J. M.: 1965, *Science* **150**, 210–212.
Shorthill, R. W. *et al.*: 1970, *Esclipse Cooling of Selected Lunar Features*, The Boeing Company, Seattle, Washington (in preparation).
Shorthill, R. W., Thompson, T. W., and Zisk, S. H.: 1972, *The Moon* **3**, 313–317.
Spurr, J. E.: 1948, *Geology Applied to Selenography*, The Rumford Press, Concord, New Hampshire.
Sukhanov, A. L., Trifanov, V. G., and Florenskiy, P. V.: 1967, 'Geologic and Plupiographic Mapping of the Moon and Some Structural Features of the Lunar Surface', *Geotectonics* **5**, 327–332, translated.
Thompson, T. W.: 1968, *Radar Studies of the Lunar Surface Emphasizing Factors Related to Selection of Landing Sites*, Final Report, Research Report RS73, Center for Radiophysics and Space Research, Cornell University, Ithaca, New York.
Thompson, T. W.: 1974, *The Moon*, this issue, p. 51.
Thompson, T. W., Pollack, J. B., Campbell, M. J., and O'Leary, B. T.: 1970, *Radio Sci.* **5**, 253–262.
Trask, N. J.: 1967, *Icarus* **6**, 270–276.
Tyler, G. L.: 1968, *J. Geophys. Res.* **73**, 7609–7620.
Tyler, G. L. and Howard, H. T.: 1973, 'Dual-Frequency Bi-Static Radar Investigation of Moon with Apollos 14 and 15', *J. Geophys. Res.*, accepted for publication.
Tyler, G. L. and Simpson, R. A.: 1970, *Radio Sci.* **5**, 263–271.
Wilhelms, D. E.: 1970, 'Summary of Lunar Stratigraphy – Telescopic Observations', *U.S. Geol.* Survey, Prof. Paper 599-F, in press.
Winter, D. F.: 1970, *Radio Sci.* **5**, 229–240.
Winter, D. F. and Saari, J. M.: 1969, *Astron. J.* **156**, 1135–1157.
Zisk, S. H., Carr, M. H., Masursky, H., Shorthill, R. W., and Thompson, T. W.: 1971, *Science* **173**, 808–812.
Zisk, S. H., Masursky, H., Milton, D. J., Schaber, G. G., Shorthill, R. W., and Thompson, T. W.: 1972, 'Apollo 16 Landing Site: Summary of Earth-Based Remote Sensing Data', NASA SP-315, pp. 29–105 to 29–110.